Analysis of transport phenomena and electrochemical reactions in a micro PEM fuel cell with serpentine gas flow channels

Maher A.R. Sadiq Al-Baghdadi

Fuel Cell Research Center, International Energy & Environment Foundation, Al-Najaf, P.O.Box 39, Iraq.

Abstract
Micro-fuel cells are considered as promising electrochemical power sources in portable electronic devices. The presence of microelectromechanical system (MEMS) technology makes it possible to manufacture the miniaturized fuel cell systems. The majority of research on micro-scale fuel cells is aimed at micro-power applications. Performance of micro-fuel cells are closely related to many factors, such as designs and operating conditions. CFD modeling and simulation for heat and mass transport in micro PEM fuel cells are being used extensively in researches and industrial applications to gain better understanding of the fundamental processes and to optimize the micro fuel cell designs before building a prototype for engineering application. In this research, full three-dimensional, non-isothermal computational fluid dynamics model of a micro proton exchange membrane (PEM) fuel cell with serpentine gas flow channels has been developed. This comprehensive model accounts for the major transport phenomena such as convective and diffusive heat and mass transfer, electrode kinetics, transport and phase-change mechanism of water, and potential fields in a micro PEM fuel cell. The model explains many interacting, complex electrochemical, and transport phenomena that cannot be studied experimentally.
Copyright © 2014 International Energy and Environment Foundation - All rights reserved.

Keywords: PEM fuel cells; Micro fuel cell with serpentine gas flow channels; Electrochemical; Heat transfer; CFD.

1. Introduction
Fuel cell system is an advanced power system for the future that is sustainable, clean and environmental friendly. Small fuel cells have provided significant advantages in portable electronic applications over conventional battery systems. Competitive costs, instant recharge, and high energy density make fuel cells ideal for supplanting batteries in portable electronic devices. Micro fuel cells belong to the category of portable fuel cells, but are used in the miniaturized electronic devices with low power, such as micro sensors. The presence of microelectromechanical system (MEMS) technology makes it possible to manufacture the miniaturized fuel cell systems for application in portable electronic devices. The majority of research on micro-scale fuel cells is aimed at micro-power applications. There are many new miniaturized applications which can only be realized if a higher energy density power source is available compared to button cells and other small batteries.

The development of physically representative models that allow reliable simulation of the processes under realistic conditions is essential to the development and optimization of fuel cells, the introduction of cheaper materials and fabrication techniques, and the design and development of novel architectures. The difficult experimental environment of fuel cell systems has stimulated efforts to develop models that could simulate and predict multi-dimensional coupled transport of reactants, heat and charged species using computational fluid dynamic (CFD) methods. These models can generally be characterized by the scope of the model. In many cases, modeling efforts focus on a specific part or parts of the fuel cell, like the cathode catalyst layer [1], the cathode electrode (gas diffusion layer plus catalyst layer) [2-4], or the membrane electrode assembly (MEA) [5]. These models are very useful in that they may include a large portion of the relevant fuel cell physics while at the same time having relatively short solution times. However, these narrowly focused models neglect important parts of the fuel cell making it impossible to get a complete picture of the phenomena governing fuel cell behavior. Models that include all parts of a fuel cell are typically two- or three-dimensional and reflect many of the physical processes occurring within the fuel cell [6–16]. In a real PEM fuel cell geometry, the gas diffusion layers are used to enhance the reaction area accessible by the reactants. The effect of using these diffusion layers is to allow a spatial distribution in the current density on the membrane in both the direction of bulk flow and the direction orthogonal to the flow but parallel to the membrane. This two-dimensional distribution cannot be modeled with the well-used two-dimensional models where the mass-transport limitation is absent in the third direction.

Berning et al. [13] used the unified approach to develop a three-dimensional model of a straight gas flow channels fuel cell. The model studied reactant concentrations, current density distributions and temperature gradients within the cell as well as water flux and species transport.

Nguyen et al. [14] developed a three-dimensional model, which accounts for mass and heat transfer, current and potential distribution within a cell using a one turn serpentine flow field. Their results show that oxygen concentration along the gas channels decrease in the direction of flow. Also, in the gas diffusion layer, the oxygen concentration is a minimum under the land area. At high current densities the oxygen is almost completely depleted under the land areas. The result is an uneven distribution of oxygen concentration along the catalyst layer resulting in local overpotentials, which vary spatially.

Um and Wang [15] used a three-dimensional model to study the effects an interdigitated flow field. The model accounted for mass transport, electrochemical kinetics, species profiles and current density distribution within the cell. Interdigitated flow fields result in forced convection of gases, which aids in liquid water removal at the cathode. This would help improve performance at high current densities when transport limitations due to excessive water production are expected. The model shows that there is little to no difference at low to medium current densities between an interdigitated flow field and a conventional flow field. However, at higher current densities, a fuel cell with an interdigitated flow field has a limiting current, which is nearly 50% greater than an equivalent cell with a conventional flow field.

Al-baghdadi [16] developed a three-dimensional model to investigate the performance of tubular-shaped PEM fuel cell. The results show that higher power densities are achieved with the tubular design mainly because of lower activation and diffusion overpotentials. Better gas replenishment at the catalyst sites in tubular design results in lower and quite uniform distribution of activation and diffusion potentials.

In this work, a multi-phase, non-isothermal, fully three-dimensional CFD model of a micro PEM fuel cell with serpentine gas flow channels is presented. The model accounts for detailed species mass transport, heat transfer in the solids as well as in the gases, potential losses in the gas diffusion layers and membrane, electrochemical kinetics, and the transport of water through the membrane.

2.1. Computational domain
The full computational domains for the micro PEM fuel cell consist of cathode and anode gas flow fields, and the MEA are shown in Figure 1.

2.2. Model equations
2.2.1. Gas flow channels
In the fuel cell channels, the gas-flow field is obtained by solving the steady-state Navier-Stokes equations, i.e. the continuity equation, the mass conservation equation for each phase yields the volume fraction (r) and along with the momentum equations the pressure distribution inside the channels. The continuity equation for the gas phase inside the channel is given by;
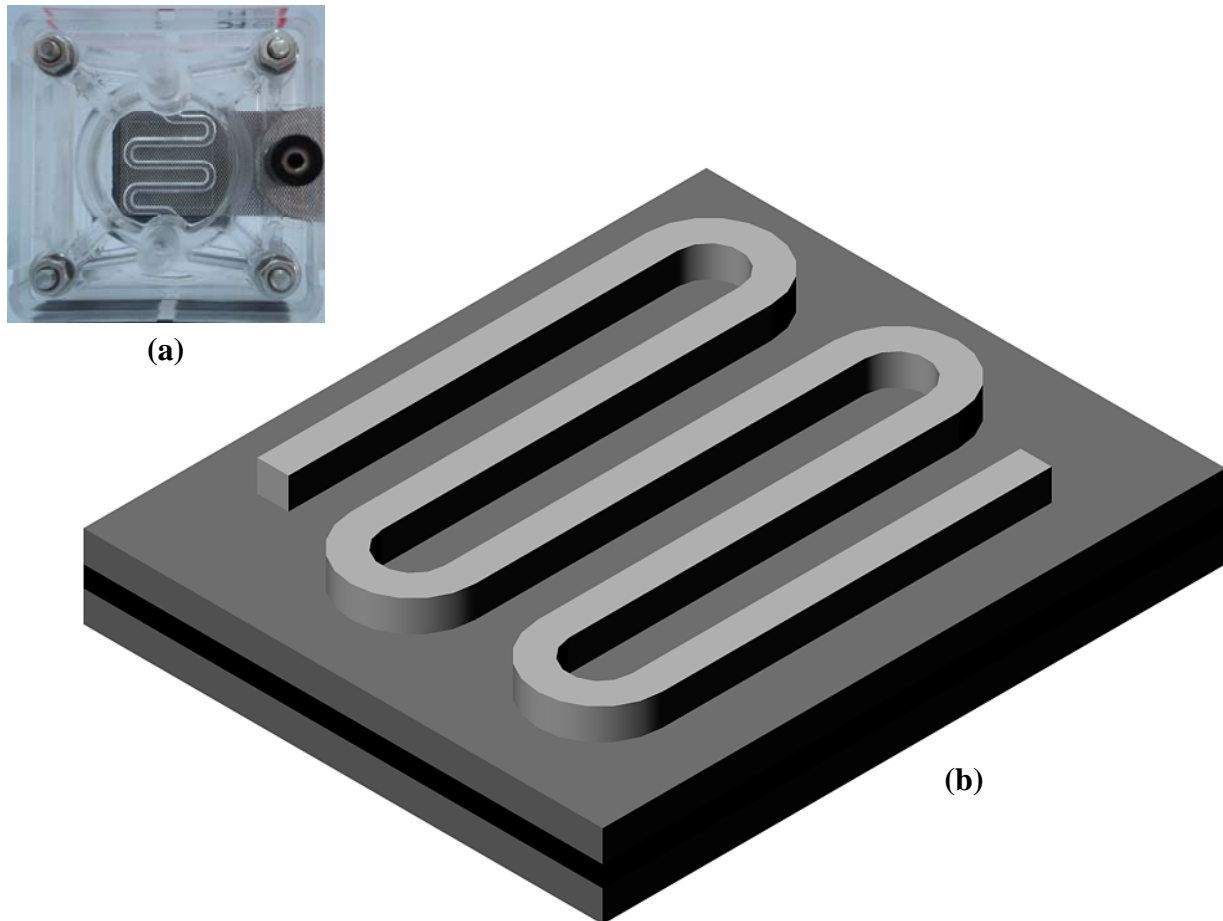
Figure 1. (a) Micro PEM fuel cell with serpentine gas flow channels, and (b) the three-dimensional computational domain of the cell.

$$\nabla \cdot \left(r_g \rho_g \mathbf{u}_g \right) = 0 \tag{1}$$

and for the liquid phase inside the channel becomes;

$$\nabla \cdot \left(r_l \rho_l \mathbf{u}_l \right) = 0 \tag{2}$$

where **u** is velocity vector [m/s], ρ is density [kg/m^3].

Two sets of momentum equations are solved in the channels, and they share the same pressure field. Under these conditions, it can be shown that the momentum equations becomes;

$$\nabla \cdot \left(\rho_g \mathbf{u}_g \otimes \mathbf{u}_g - \mu_g \nabla \mathbf{u}_g \right) = -\nabla r_g \left(P + \frac{2}{3} \mu_g \nabla \cdot \mathbf{u}_g \right) + \nabla \cdot \left[\mu_g \left(\nabla \mathbf{u}_g \right)^T \right] \tag{3}$$

$$\nabla \cdot \left(\rho_l \mathbf{u}_l \otimes \mathbf{u}_l - \mu_l \nabla \mathbf{u}_l \right) = -\nabla r_l \left(P + \frac{2}{3} \mu_l \nabla \cdot \mathbf{u}_l \right) + \nabla \cdot \left[\mu_l \left(\nabla \mathbf{u}_l \right)^T \right] \tag{4}$$

where P is pressure (Pa), μ is viscosity [kg/(m·s)].

The mass balance is described by the divergence of the mass flux through diffusion and convection. Multiple species are considered in the gas phase only, and the species conservation equation in multi-component, multi-phase flow can be written in the following expression for species i;

$$\nabla \cdot \left[\begin{array}{c} - r_g \rho_g y_i \sum_{j=1}^{N} D_{ij} \frac{M}{M_j} \left[\left(\nabla y_j + y_j \frac{\nabla M}{M} \right) + \left(x_j - y_j \right) \frac{\nabla P}{P} \right] + \\ r_g \rho_g y_i \cdot \mathbf{u}_g + D_i^T \frac{\nabla T}{T} \end{array} \right] = 0 \tag{5}$$

where T is temperature (K), y is mass fraction, x is mole fraction, D is diffusion coefficient [m^2/s].

Subscript i denotes oxygen at the cathode side and hydrogen at the anode side, and j is water vapour in both cases. Nitrogen is the third species at the cathode side.

The Maxwell-Stefan diffusion coefficients of any two species are dependent on temperature and pressure. They can be calculated according to the empirical relation based on kinetic gas theory [17];

$$D_{ij} = \frac{T^{1.75} \times 10^{-3}}{P\left[\left(\sum_k V_{ki}\right)^{1/3} + \left(\sum_k V_{kj}\right)^{1/3}\right]^2} \left[\frac{1}{M_i} + \frac{1}{M_j}\right]^{1/2} \tag{6}$$

In this equation, the pressure is in atm and the binary diffusion coefficient Dij is in [cm^2/s].
The values for $\left(\sum V_{ki}\right)$ are given by Fuller et al. [17].

The temperature field is obtained by solving the convective energy equation;

$$\nabla \cdot \left(r_g \left(\rho_g Cp_g \mathbf{u}_g T - k_g \nabla T\right)\right) = 0 \tag{7}$$

where Cp is specific heat capacity [J/(kg.K)], k is gas thermal conductivity [W/(m.K)].
The gas phase and the liquid phase are assumed to be in thermodynamic equilibrium; hence, the temperature of the liquid water is the same as the gas phase temperature.

2.2.2. Gas diffusion layers
The physics of multiple phases through a porous medium is further complicated here with phase change and the sources and sinks associated with the electrochemical reaction. The equations used to describe transport in the gas diffusion layers are given below. Mass transfer in the form of evaporation $\left(\dot{m}_{phase} > 0\right)$ and condensation $\left(\dot{m}_{phase} < 0\right)$ is assumed, so that the mass balance equations for both phases are;

$$\nabla \cdot \left((1 - sat)\rho_g \varepsilon \mathbf{u}_g\right) = \dot{m}_{phase} \tag{8}$$

$$\nabla \cdot \left(sat.\rho_l \varepsilon \mathbf{u}_l\right) = \dot{m}_{phase} \tag{9}$$

where sat is saturation, ε is porosity
The momentum equation for the gas phase reduces to Darcy's law, which is, however, based on the relative permeability for the gas phase (KP). The relative permeability accounts for the reduction in pore space available for one phase due to the existence of the second phase [18].
The momentum equation for the gas phase inside the gas diffusion layer becomes;

$$\mathbf{u}_g = -(1 - sat)Kp.\nabla P / \mu_g \tag{10}$$

where KP is hydraulic permeability [m^2].

Two liquid water transport mechanisms are considered; shear, which drags the liquid phase along with the gas phase in the direction of the pressure gradient, and capillary forces, which drive liquid water from high to low saturation regions [18]. Therefore, the momentum equation for the liquid phase inside the gas diffusion layer becomes;

$$\mathbf{u}_l = -\frac{KP_l}{\mu_l}\nabla P + \frac{KP_l}{\mu_l}\frac{\partial P_c}{\partial sat}\nabla sat \tag{11}$$

where Pc is capillary pressure [Pa].

The functional variation of capillary pressure with saturation is prescribed following Leverett [18] who has shown that;

$$P_c = \tau\left(\frac{\varepsilon}{KP}\right)^{1/2}\left(1.417(1 - sat) - 2.12(1 - sat)^2 + 1.263(1 - sat)^3\right) \tag{12}$$

where τ is surface tension [N/m].

The liquid phase consists of pure water, while the gas phase has multi components. The transport of each species in the gas phase is governed by a general convection-diffusion equation in conjunction which the Stefan-Maxwell equations to account for multi species diffusion;

$$\nabla \cdot \left[\begin{array}{l} -(1-sat)\rho_g \varepsilon y_i \sum_{j=1}^{N} D_{ij} \frac{M}{M_j} \left[\left(\nabla y_j + y_j \frac{\nabla M}{M} \right) + (x_j - y_j) \frac{\nabla P}{P} \right] + \\ (1-sat)\rho_g \varepsilon y_i \cdot \mathbf{u}_g + \varepsilon D_i^T \frac{\nabla T}{T} \end{array} \right] = \dot{m}_{phase} \tag{13}$$

In order to account for geometric constraints of the porous media, the diffusivities are corrected using the Bruggemann correction formula [14];

$$D_{ij}^{eff} = D_{ij} \times \varepsilon^{1.5} \tag{14}$$

The heat transfer in the gas diffusion layers is governed by the energy equation as follows;

$$\nabla \cdot \left((1-sat)(\rho_g \varepsilon Cp_g \mathbf{u}_g T - k_{eff,g} \varepsilon \nabla T) \right) = \varepsilon \beta (T_{solid} - T) - \varepsilon \dot{m}_{phase} \Delta H_{evap} \tag{15}$$

where *keff* is effective electrode thermal conductivity [W/(m·K)]; the term [εβ(Tsolid−T)], on the right hand side, accounts for the heat exchange to and from the solid matrix of the GDL. The gas phase and the liquid phase are assumed to be in thermodynamic equilibrium, i.e., the liquid water and the gas phase are at the same temperature.

The potential distribution in the gas diffusion layers is governed by;

$$\nabla \cdot (\lambda_e \nabla \phi) = 0 \tag{16}$$

where *λe* is electrode electronic conductivity [S/m].

In order to account for the magnitude of phase change inside the GDL, expressions are required to relate the level of over- and undersaturation as well as the amount of liquid water present to the amount of water undergoing phase change. In the present work, the procedure of Berning and Djilali [18] was used to account for the magnitude of phase change inside the GDL.

2.2.3. Catalyst layers
The catalyst layer is treated as a thin interface, where sink and source terms for the reactants are implemented. Due to the infinitesimal thickness, the source terms are actually implemented in the last grid cell of the porous medium. At the cathode side, the sink term for oxygen is given by;

$$S_{O_2} = -\frac{M_{O_2}}{4F} i_c \tag{17}$$

where F is Faraday's constant (96487 [C/mole]), i_c is cathode local current density [A/m²], M is molecular weight [kg/mole].

Whereas the sink term for hydrogen is specified as;

$$S_{H_2} = -\frac{M_{H_2}}{2F} i_a \tag{18}$$

where i_a is anode local current density [A/m²]

The production of water is modelled as a source terms, and hence can be written as;

$$S_{H_2O} = \frac{M_{H_2O}}{2F} i_c \tag{19}$$

The generation of heat in the cell is due to entropy changes as well as irreversibility's due to the activation overpotential [19];

$$\dot{q} = \left[\frac{T(-\Delta s)}{n_e F} + \eta_{act} \right] i \tag{20}$$

where $\dot{q}$ is heat generation [W/m²], ne is number of electrons transfer, *s* is specific entropy [J/(mole.K)], ηact is activation overpotential (V).
The local current density distribution in the catalyst layers is modelled by the Butler-Volmer equation [18, 19];

$$i_c = i_{o,c}^{ref}\left(\frac{C_{O_2}}{C_{O_2}^{ref}}\right)\left[\exp\left(\frac{\alpha_a F}{RT}\eta_{act,c}\right)+\exp\left(-\frac{\alpha_c F}{RT}\eta_{act,c}\right)\right] \tag{21}$$

$$i_a = i_{o,a}^{ref}\left(\frac{C_{H_2}}{C_{H_2}^{ref}}\right)^{1/2}\left[\exp\left(\frac{\alpha_a F}{RT}\eta_{act,a}\right)+\exp\left(-\frac{\alpha_c F}{RT}\eta_{act,a}\right)\right] \tag{22}$$

where C_{H_2} is local hydrogen concentration [mole/m^3], $C_{H_2}^{ref}$ is reference hydrogen concentration [mole/m^3], C_{O_2} is local oxygen concentration [mole/m^3], $C_{O_2}^{ref}$ is reference oxygen concentration [mole/m^3], $i_{o,a}^{ref}$ is anode reference exchange current density, $i_{o,c}^{ref}$ is cathode reference exchange current density, R is universal gas constant (8.314 [J/(mole·K)]), αa is charge transfer coefficient, anode side, and αc is charge transfer coefficient, cathode side.

2.2.4. Membrane
The balance between the electro-osmotic drag of water from anode to cathode and back diffusion from cathode to anode yields the net water flux through the membrane;

$$N_W = n_d M_{H_2O}\frac{i}{F}-\nabla\cdot(\rho D_W \nabla c_W) \tag{23}$$

where Nw is net water flux across the membrane [kg/(m^2·s)], nd is electro-osmotic drag coefficient.

The water diffusivity in the polymer can be calculated as follow [12];

$$D_W = 1.3\times10^{-10}\exp\left[2416\left(\frac{1}{303}-\frac{1}{T}\right)\right] \tag{24}$$

The variable c_W represents the number of water molecules per sulfonic acid group (i.e. mol H_2O/equivalent SO_3^{-1}). The water content in the electrolyte phase is related to water vapour activity via [6, 7];

$$
\begin{aligned}
c_W &= 0.043+17.81a-39.85a^2+36.0a^3 &&(0 < a \le 1)\\
c_W &= 14.0+1.4(a-1) &&(1 < a \le 3)\\
c_W &= 16.8 &&(a \ge 3)
\end{aligned}
\tag{25}
$$

The water vapour activity a given by;
$$a = x_W P/P_{sat} \tag{26}$$

Heat transfer in the membrane is governed by;
$$\nabla\cdot(k_{mem}\cdot\nabla T)=0 \tag{27}$$
where k_{mem} is membrane thermal conductivity [W/(m·K)].

The potential loss in the membrane is due to resistance to proton transport across membrane, and is governed by;
$$\nabla\cdot(\lambda_m \nabla\phi)=0 \tag{28}$$
where λ_m is membrane ionic conductivity [S/m].

2.2.5. Potential drop across the cell
Useful work (electrical energy) is obtained from a fuel cell only when a current is drawn, but the actual cell potential, (E_{cell}), is decreased from its equilibrium thermodynamic potential, (E), because of irreversible losses. The various irreversible loss mechanisms which are often called overpotentials, (η), are defined as the deviation of the cell potential, (E_{cell}), from the equilibrium thermodynamic potential

(E). The cell potential (E_{cell}) is obtained by subtracting all overpotentials (η) (losses) from the equilibrium thermodynamic potential (E) as the following expression;

$$E_{cell} = E - \eta_{act} - \eta_{ohm} - \eta_{mem} - \eta_{Diff} \tag{29}$$

The equilibrium potential is determined using the Nernst equation [16];

$$E = 1.229 - 0.83 \times 10^{-3}(T - 298.15) + 4.3085 \times 10^{-5}T\left[\ln(P_{H_2}) + \frac{1}{2}\ln(P_{O_2})\right] \tag{30}$$

2.2.5.1. Activation Overpotential

Activation overpotential (η_{act}) arises from the kinetics of charge transfer reaction across the electrode-electrolyte interface. In other words, a portion of the electrode potential is lost in driving the electron transfer reaction. Activation overpotential is directly related to the nature of the electrochemical reactions and represents the magnitude of activation energy, when the reaction propagates at the rate demanded by the current. The activation overpotential can be divided into the anode and cathode overpotentials. The anode and cathode activation overpotentials are calculated from Butler-Volmer equation (21 and 22).

2.2.5.2. Ohmic Overpotential in Gas Diffusion Layers

The Ohmic overpotential (η_{ohm}) is the potential loss due to current conduction through the anode and cathode gas diffusion layers, and can be modeled by equation (16).

2.2.5.3. Membrane Overpotential

The membrane overpotential (η_{mem}) is related to the fact that an electric field is necessary in order to maintain the motion of the hydrogen protons through the membrane. This field is provided by the existence of a potential gradient across the cell, which is directed in the opposite direction from the outer field that gives us the cell potential, and thus has to be subtracted. The overpotential in membrane is calculated from the potential equation (28).

2.2.5.4. Diffusion Overpotential

Diffusion overpotential (η_{Diff}) is caused by mass transfer limitations on the availability of the reactants near the electrodes. The electrode reactions require a constant supply of reactants in order to sustain the current flow. When the diffusion limitations reduce the availability of a reactant, part of the available reaction energy is used to drive the mass transfer, thus creating a corresponding loss in output voltage. Similar problems can develop if a reaction product accumulates near the electrode surface and obstructs the diffusion paths or dilutes the reactants. Mass transport loss becomes significant when the fuel cell is operated at high current density. This is created by the concentration gradient due to the consumption of oxygen or fuel at the electrodes. The mass transport loss at the anode is negligible compared to that at the cathode. At the limiting current density, oxygen at the catalyst layer is depleted and no more current increase can be obtained from the fuel cell. This is responsible for the sharp decline in potential at high current densities. To reduce mass transport loss, the cathode is usually run at high pressure. The anode and cathode diffusion overpotentials are calculated from the following equations [19];

$$\eta_{Diff,c} = \frac{RT}{2F}\ln\left(1 - \frac{i_c}{i_{L,c}}\right) \tag{31}$$

$$\eta_{Diff,a} = \frac{RT}{2F}\ln\left(1 - \frac{i_a}{i_{L,a}}\right) \tag{32}$$

$$i_{L,c} = \frac{2FD_{O_2}C_{O_2}}{\delta_{GDL}} \tag{33}$$

$$i_{L,a} = \frac{2FD_{H_2}C_{H_2}}{\delta_{GDL}} \tag{34}$$

where $i_{L,c}$ and $i_{L,a}$ are cathode and anode local limiting current density [A/m^2], δ_{GDL} is the gas diffusion layer thickness [m], D is the diffusion coefficients [m^2/s].
The diffusivity of oxygen and hydrogen are calculated from the following equations [19];

$$D_{O_2} = 3.2 \times 10^{-5} \left(\frac{T}{353}\right)^{3/2} \left(\frac{101325}{P}\right) \tag{35}$$

$$D_{H_2} = 1.1 \times 10^{-4} \left(\frac{T}{353}\right)^{3/2} \left(\frac{101325}{P}\right) \tag{36}$$

2.2.6. Cell power and efficiency
Once the cell potential is determined for a given current density, the output power density is found as;
$$W_{cell} = I.E_{cell} \tag{37}$$
where I is the cell operating (nominal) current density (A/m^2).
The thermodynamic efficiency of the cell can be determined as [19];

$$E_{fc} = \frac{2E_{cell}F}{M_{H_2}.LHV_{H_2}} \tag{38}$$

where LHV_{H2} is the lower heating value of hydrogen [J/kg]

2.3. Boundary conditions
Boundary conditions are specified at all external boundaries of the computational domain as well as boundaries for various mass and scalar equations inside the computational domain.

2.3.1. Inlets
The inlet values at the anode and cathode are prescribed for the velocity, temperature and species concentrations (Dirichlet boundary conditions). The inlet velocity is a function of the desired current density, the geometrical area of the membrane, the channel cross-section area, and stoichiometric flow ratio. The inlet velocities of air and fuel are calculated according to [20]:

$$u_{in,c} = \zeta_c \frac{I}{4F} A_{MEA} \frac{1}{x_{O_2,in}} \frac{RT_{in,c}}{P_c} \frac{1}{A_{ch}} \tag{39}$$

$$u_{in,a} = \zeta_a \frac{I}{2F} A_{MEA} \frac{1}{x_{H_2,in}} \frac{RT_{in,a}}{P_a} \frac{1}{A_{ch}} \tag{40}$$

where A_{MEA} is the area of the MEA [m^2], A_{ch} is the cross sectional area of flow channel [m^2], and ξ is the stoichiometric flow ratio.

2.3.2. Outlets
At the outlets of the gas-flow channels, only the pressure is being prescribed as the desired electrode pressure; for all other variables, the gradient in the flow direction is assumed to be zero (Neumann boundary conditions).

2.3.3. External surfaces
At the external surfaces of the cell, temperature is specified and zero heat flux is applied at the surface of the conducting boundary surfaces.

2.3.4. Interfaces inside the computational domain
Combinations of Dirichlet and Neumann boundary conditions are used to solve the electronic and protonic potential equations. Dirichlet boundary conditions are applied at the land area (interface between the bipolar plates and the gas diffusion layers). Neumann boundary conditions are applied at the interface between the gas channels and the gas diffusion layers to give zero potential flux into the gas channels. Similarly, the protonic potential field requires a set of potential boundary condition and zero flux boundary condition at the anode catalyst layer interface and cathode catalyst layer interface respectively.

2.4. Computational procedure
2.4.1. Computational grid

The governing equations were discretized using a finite volume method and solved using a multi-physics general-purpose computational fluid dynamic (CFD) code. The computational domains are divided into a finite number of control volumes (cells). All variables are stored at the centroid of each cell. Interpolation is used to express variable values at the control volume surface in terms of the control volume center values. Stringent numerical tests were performed to ensure that the solutions were independent of the grid size. A computational quadratic mesh consisting of a total of 11556 nodes and 59814 meshes was found to provide sufficient spatial resolution (Figure 2). The coupled set of equations was solved iteratively, and the solution was considered to be convergent when the relative error was less than 1.0×10^{-6} in each field between two consecutive iterations. The geometric and the base case operating conditions are listed in Table 1. Values of the electrochemical transport parameters for the base case operating conditions are taken from reference [20] and are listed in Table 2.

2.4.2. Solution algorithm

The solution begins by specifying a desired current density of the cell to be used for calculating the inlet flow rates at the anode and cathode sides. An initial guess of the activation overpotential is obtained from the desired current density using the Butler-Volmer equation. Then follows by computing the flow fields for velocities u,v,w, and pressure P. Once the flow field is obtained, the mass fraction equations are solved for the mass fractions of oxygen, hydrogen, water vapor, and nitrogen. Scalar equations are solved last in the sequence of the transport equations for the temperature field in the cell and potential fields in the gas diffusion layers and the membrane. The local current densities are solved based on the Butler-Volmer equation. After the local current densities are obtained, the local activation overpotentials can be readily calculated from the Butler-Volmer equation. The local activation overpotentials are updated after each global iterative loop. Convergence criteria are then performed on each variable and the procedure is repeated until convergence. The properties and then source terms are updated after each global iterative loop based on the new local gas composition and temperature. The strength of the current model is clearly to perform parametric studies and explore the impact of various parameters on the transport mechanisms and on fuel cell performance. The new feature of the algorithm developed in this work is its capability for accurate calculation of the local activation overpotentials, which in turn results in improved prediction of the local current density distribution. The flow diagram of the algorithm is shown in Figure 3.
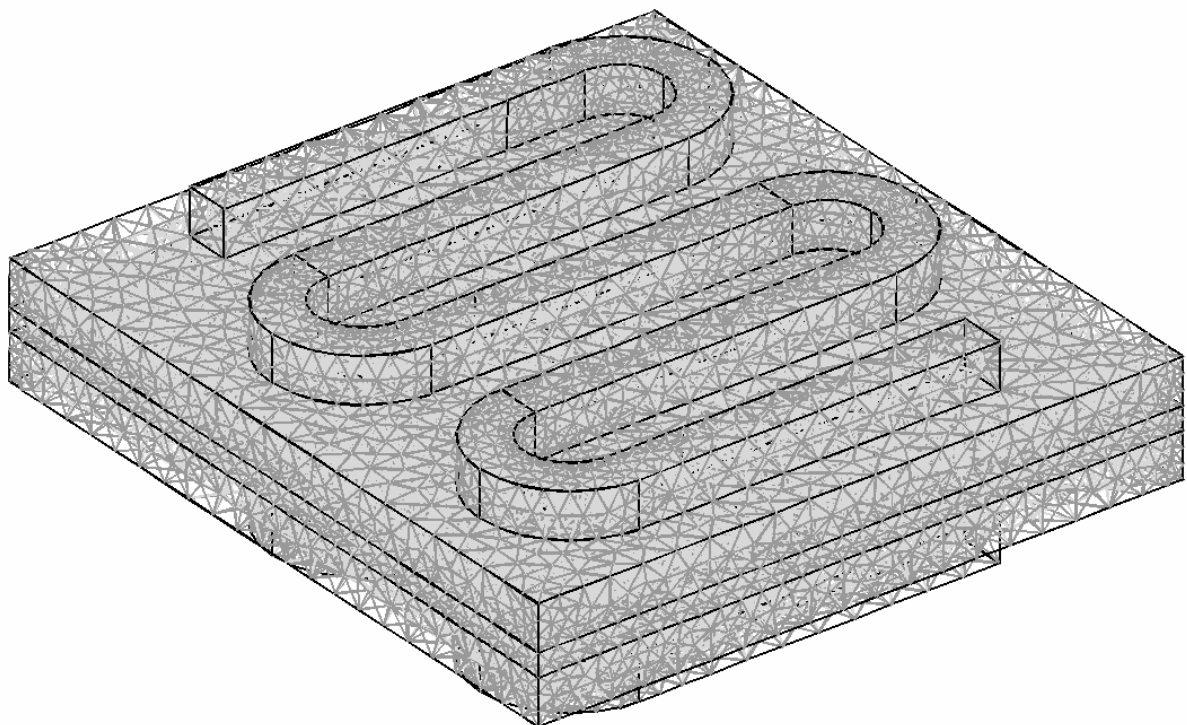

Figure 2. Computational mesh for micro PEM fuel cell with serpentine gas flow channels.

Table 1. Geometrical and operational parameters for base case conditions.

Parameter	Symbol	Value
Cell length	L_{cell}	5000 μm
Cell width	W_{cell}	5000 μm
Gas channel width	W	300 μm
Gas channel height	H	300 μm
Gas diffusion layer thickness	δ_{GDL}	260 μm
Wet membrane thickness (Nafion® 117)	δ_{mem}	50 μm
Catalyst layer thickness	δ_{CL}	28.7 μm
Hydrogen reference mole fraction	$x_{H_2}^{ref}$	0.84639
Oxygen reference mole fraction	$x_{O_2}^{ref}$	0.17774
Anode pressure	P_a	1e5 Pa
Cathode pressure	P_c	1e5 Pa
Inlet fuel and air temperature	T_{cell}	323.15 K
Relative humidity of inlet fuel and air	ψ	100 %
Air stoichiometric flow ratio	ξ_c	2
Fuel stoichiometric flow ratio	ξ_a	2

Table 2. Electrode and membrane parameters for base case operating conditions.

| Parameter	Symbol	Value
Electrode porosity	ε	0.4
Electrode electronic conductivity	λ_e	100 S/m
Membrane ionic conductivity (Nafion®117)	λ_m	17.1223 S/m
Transfer coefficient, anode side	α_a	0.5
Transfer coefficient, cathode side	α_c	1
Cathode reference exchange current density	$i_{o,c}^{ref}$	1.8081e-3 A/m^2
Anode reference exchange current density	$i_{o,a}^{ref}$	2465.598 A/m^2
Electrode thermal conductivity	k_{eff}	1.3 W/m.K
Membrane thermal conductivity	k_{mem}	0.455 W/m.K
Electrode hydraulic permeability	kp	1.76e-11 m^2
Entropy change of cathode side reaction	ΔS	-326.36 J/mol.K
Heat transfer coef. between solid and gas phase	β	4e6 W/m^3
Protonic diffusion coefficient	D_{H^+}	4.5e-9 m^2/s
Fixed-charge concentration	c_f	1200 mol/m^3
Fixed-site charge	z_f	-1
Electro-osmotic drag coefficient	n_d	2.5
Droplet diameter	D_{drop}	1e-8 m
Condensation constant	C	1e-5
Scaling parameter for evaporation	ϖ	0.01
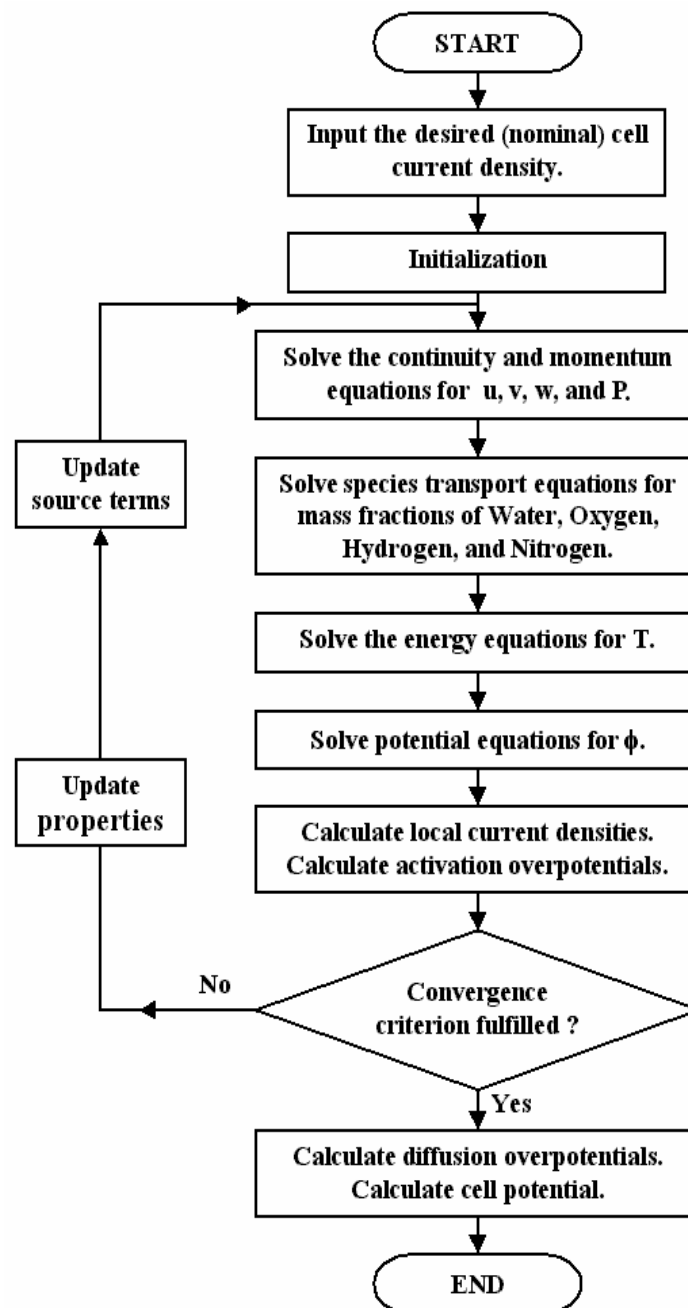
Figure 3. Flow diagram of the solution procedure used.

3. Results and discussion

Performance curves for micro fuel cell are shown in Figure 4. The multi-phase model is validated by comparing model results to experimental data. It can be seen that the modelling results compare well with the experimental data. The importance of phase change to the accurate modelling of fuel cell performance is illustrated. By including the effects of phase change, the current model is able to more closely simulate performance, especially in the region where mass transport effects begin to dominate. In order to gain some insight into the micro-structured PEM fuel cell, the oxygen and hydrogen distribution, local current densities, and temperature distribution are plotted in Figures 5-9, respectively, at 0.3 A/cm^2 nominal current density.

The velocity profiles in the mid-plane of the cathode (red) and anode (green) gas flow channels are shown in Figure 5. The velocity exhibits a laminar fully developed profile where the highest velocity is located at the centre of the channels and this profile is maintained until the end of the channels. However, the velocity scale in the anode gas flow channel is several orders of magnitude smaller than that in the cathode gas flow channel. This is because the molar fraction of the hydrogen of the incoming humid gas

is greater than that of oxygen, and hence, the inlet velocity at the anode gas flow channel is smaller than that at cathode gas flow channel.

The detailed distribution of oxygen weight fraction is shown in Figures 6 and 7. In the GDL, oxygen concentration under the land area is smaller than that under the air inlet area. The concentration of oxygen at the catalyst layer is balanced by the oxygen that is being consumed and the amount of oxygen that diffuses towards the catalyst layer driven by the concentration gradient. The lower diffusivity of the oxygen along with the low concentration of oxygen in ambient air results in noticeable oxygen depletion under the land areas. However, the decrease in molar concentration of the hydrogen under the land areas is smaller than for the oxygen in cathode side due to the higher diffusivity of the hydrogen.

Due to the relatively low diffusivity of the oxygen compared with that of the hydrogen, the cathode operation conditions usually determine the limiting current density. This is because an increase in current density corresponds to an increase in oxygen consumption.

Figure 8 shows the local current density distribution at the cathode side catalyst layer. The local current densities have been normalized by the nominal current density in each case (i.e. ic/I). The local current density of the cathode side reaction depends directly on the oxygen concentration. The diffusion of the oxygen towards the catalyst layer is the main impediment for reaching high current densities. Therefore, it can be seen that the local current density under the land areas a noticeable decrease takes place. A high fraction of the current is generated at the catalyst layer that lies beneath the air inlet area, leading to under-utilization of the catalyst under the land areas. This can lead to local hot spots inside the membrane electrode assembly. These hot spots can lead to a further drying out of the membrane, thus increasing the electric resistance, which in turn leads to more heat generation and can lead to a failure of the membrane. Thus, it is important to keep the current density relatively even throughout the cell. For optimal fuel cell performance, a uniform current density generation is desirable, and this could only be achieved with a non-uniform catalyst distribution, possibly in conjunction with non-homogeneous gas diffusion layers.

The temperature distribution inside the fuel cell has important effects on nearly all transport phenomena, and knowledge of the magnitude of temperature increases due to irreversibilities might help prevent failure. Figure 9 shows the distribution of the temperature at the cathode side catalyst layer. The temperature peak appears in the cathode catalyst layer near the inlet area, implying that major heat generation takes place in the region. For an optimum fuel cell performance, and in order to avoid large temperature gradients inside the fuel cell, it is desirable to achieve a uniform current density distribution inside the cell.
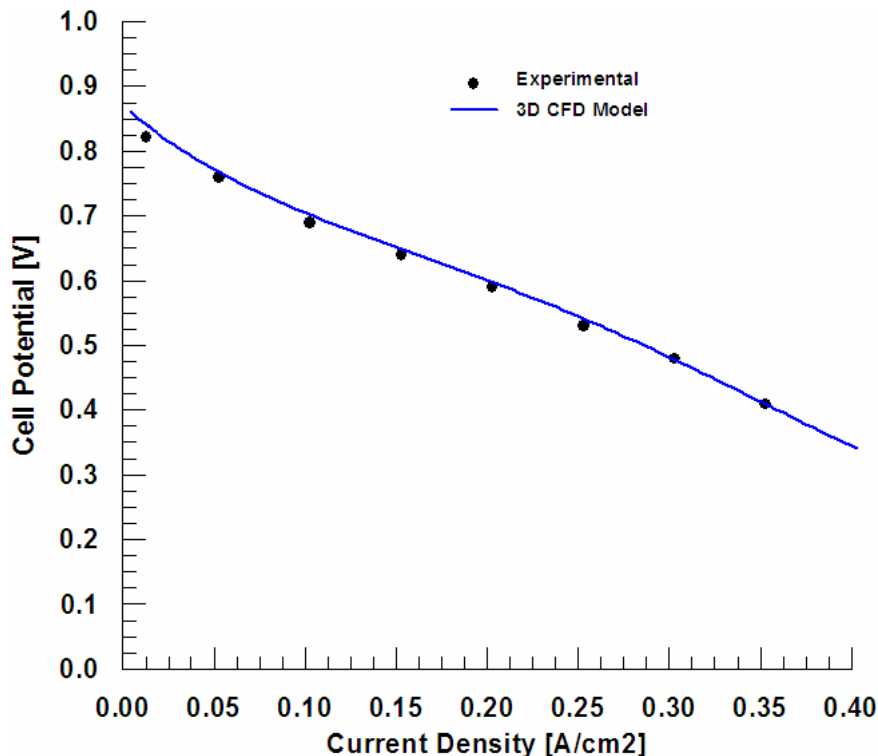

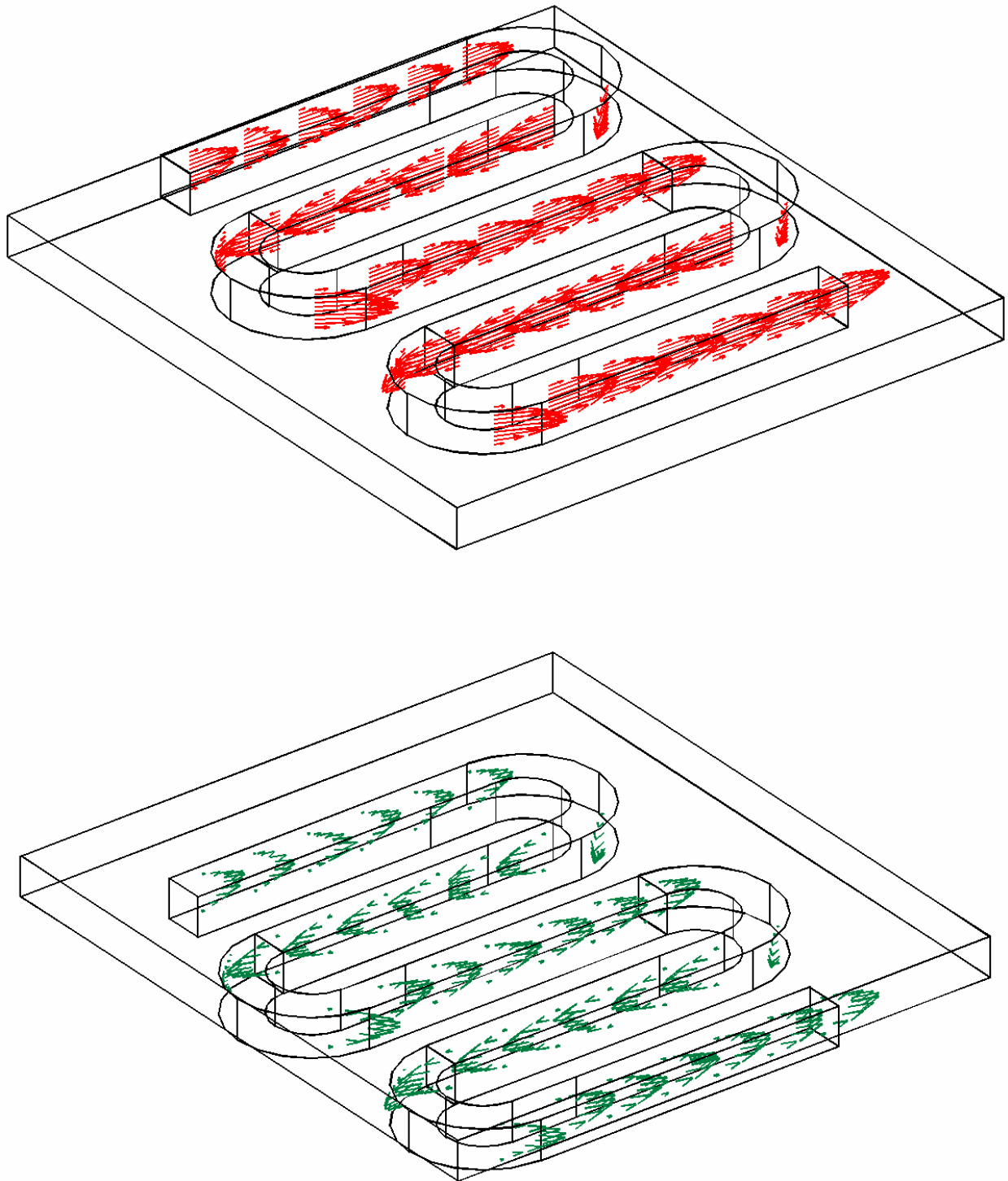Figure 4. Comparison of the model and the experimental polarization curves.

Figure 5. Velocity profiles in the mid-plane of the cathode (red) and anode (green) gas flow channels.
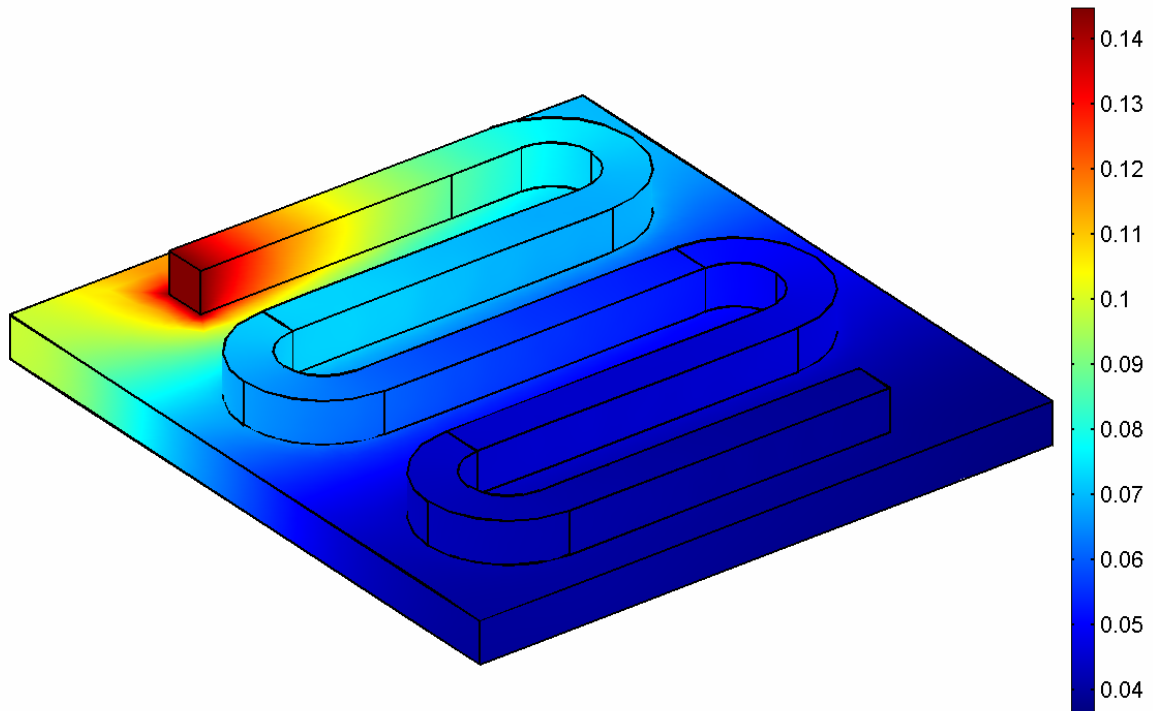
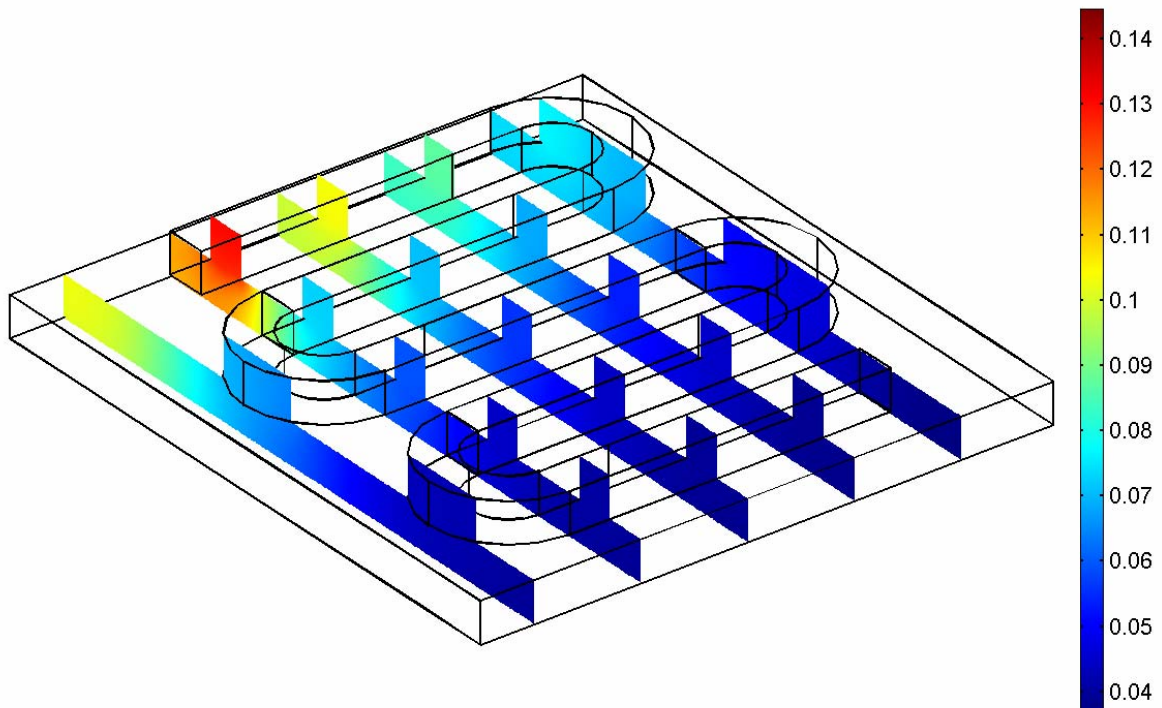Figure 6. Oxygen weight fraction distribution.

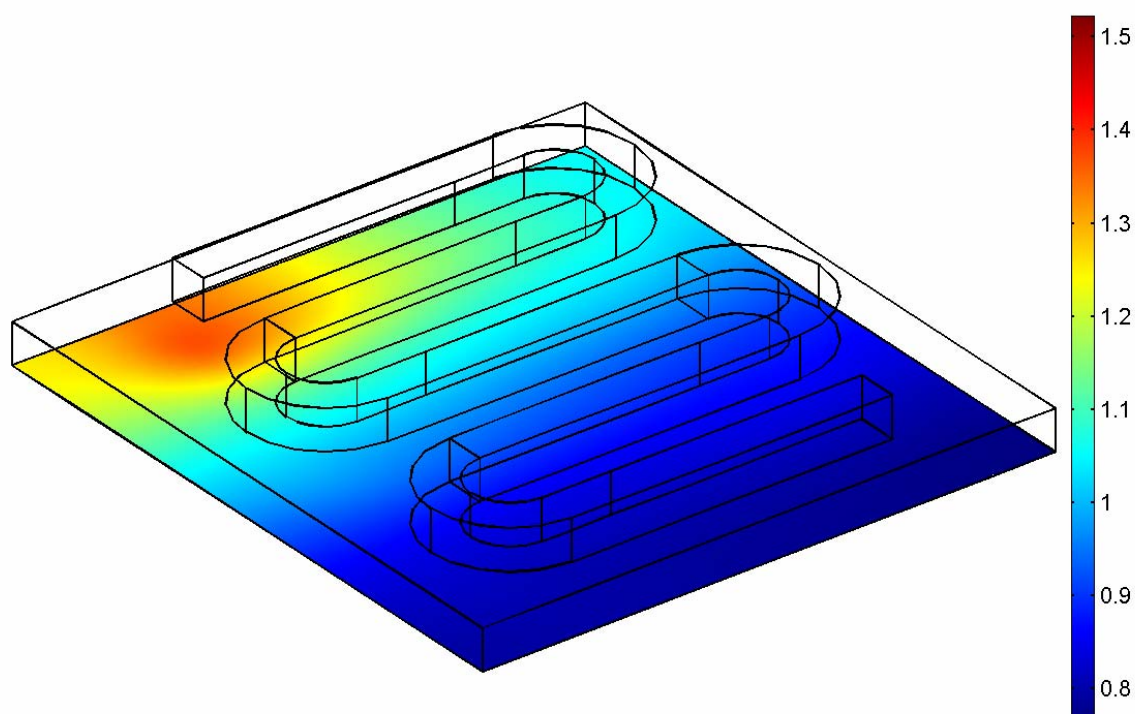Figure 7. Oxygen weight fraction distribution..

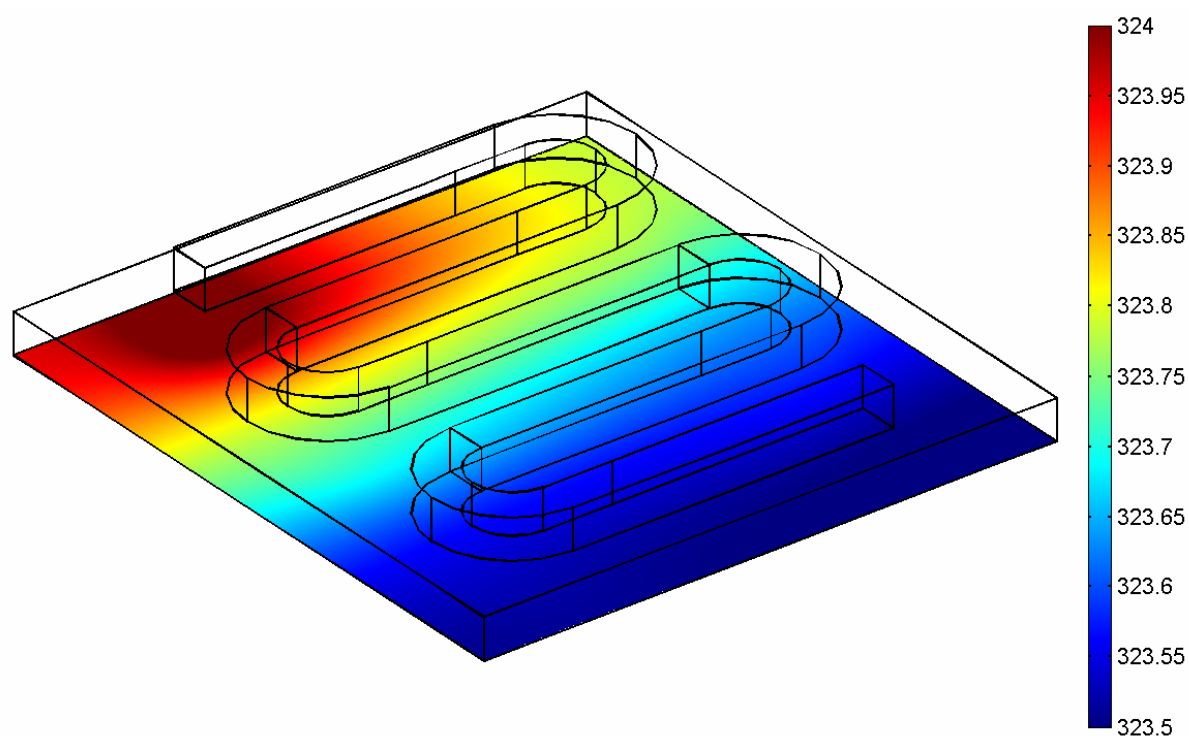Figure 8. Dimensionless local current density distribution (ic/I) at cathode side catalyst layer.

Figure 9. Temperature distribution at the cathode side catalyst layer.

4. Conclusion

Every component of the micro-fuel cells plays important role in their performance. Full three-dimensional, non-isothermal computational fluid dynamics model of all components of a micro proton exchange membrane (PEM) fuel cell with serpentine gas flow channels has been developed and used to investigate the cell performance. This comprehensive model accounts for the major transport phenomena such as convective and diffusive heat and mass transfer, electrode kinetics, transport and phase-change mechanism of water, and potential fields in a micro PEM fuel cell with serpentine gas flow channels. The model is shown to be able to: understand the many interacting, complex electrochemical and transport

phenomena that cannot be studied experimentally; identify limiting steps and components; and provide a computer-aided tool for the design and optimization of future fuel cells to improve their lifetime with a much higher power density and lower cost.

The analysis offers valuable physical insight towards design of a cell and a cell stack, to be considered in a future study. Finally, the development of physically representative models that allow reliable simulation of the processes under realistic conditions is essential to the development and optimization of micro fuel cells, improve long-term performance and lifetime, the introduction of cheaper materials and fabrication techniques, and the design and development of novel architectures.

References
[1]   Jeng, K.T., Kuo, C.P. and Lee, S.F. Modeling the catalyst layer of a PEM fuel cell cathode using a dimensionless approach. J. Power Sources, 2004, 128(2), 145–151.
[2]   Jaouen, F., Lindbergh, G., and Sundholm, G. Investigation of mass-transport limitations in the solid polymer fuel cell cathode. J. Electrochem. Soc., 2002, 149(4), A437-A447.
[3]   Grujicic, M., and Chittajallu, K.M. Optimization of the cathode geometry in polymer electrolyte membrane (PEM) fuel cells. Chemical Engineering Science, 2004, 59(24), 5883–5895.
[4]   Grujicic, M., Zhao, C.L., Chittajallu, K.M., and Ochterbeck, J.M. Cathode and interdigitated air distributor geometry optimization in polymer electrolyte membrane (PEM) fuel cells. Materials Science and Engineering B, 2004, 108(3), 241–252.
[5]   Francesco,De., Arato,E., Costa,P. Transport phenomena in membranes of PEMFC applications: an analytical approach to the calculation of membrane resistance. J.Power Sources, 2004, 132(1-2), 127-134.
[6]   Maher A.R. Sadiq Al-Baghdadi. Modeling optimizes PEM fuel cell durability using three-dimensional multi-phase computational fluid dynamics model. International Journal of Energy and Environment IJEE, 2010; 1(3), 375-398.
[7]   Maher A.R. Sadiq Al-Baghdadi. Mechanical behaviour of PEM fuel cell catalyst layers during regular cell operation. International Journal of Energy and Environment, 2010; 1(6), 927-936.
[8]   Maher A.R. Sadiq Al-Baghdadi. A CFD analysis on the effect of ambient conditions on the hygro-thermal stresses distribution in a planar ambient air-breathing PEM fuel cell. International Journal of Energy and Environment, 2011; 2(4), 589-604.
[9]   F. Brèque, J. Ramousse, Y. Dubé, K. Agbossou, P. Adzakpa. Sensibility study of flooding and drying issues to the operating conditions in PEM Fuel Cells. International Journal of Energy and Environment IJEE, 2010; 1(1), 1-20.
[10]   Maher A.R. Sadiq Al-Baghdadi. Optimal design of PEM fuel cells to generate maximum power: A CFD study. International Journal of Energy and Environment, 2011; 2(6), 953-962.
[11]   Maher A.R. Sadiq Al-Baghdadi. Novel design of a compacted micro-structured air-breathing PEM fuel cell as a power source for mobile phones. International Journal of Energy and Environment IJEE, 2010; 1(4), 555-572.
[12]   Siegel,N.P., Ellis,M.W., Nelson,D.J., Spakovsky,M.R. von. A two-dimensional computational model of a PEMFC with liquid water transport. J. Power Sources, 2004, 128(2), 173–184.
[13]   Berning, T., Lu, D.M., and Djilali, N. Three-Dimensional Computational Analysis of Transport Phenomena in a PEM Fuel Cell. J. Power Sources, 2002, 106(1-2), 284-294.
[14]   Nguyen, P.T., Berning, T., and Djilali, N. Computational Model of a PEM Fuel Cell with Serpentine Gas Flow Channels. J. Power Sources, 2004, 130(1-2), 149-157.
[15]   Sukkee, Um., and Wang, C.Y. Three-dimensional analysis of transport and electrochemical reactions in polymer electrolyte fuel cells. J. Power Sources, 2004, 125(2), 40–51.
[16]   Maher A.R. Sadiq Al-Baghdadi. A CFD analysis of transport phenomena and electrochemical reactions in a tubular-shaped PEM fuel cell. Int. J. of Energy and Environment, 2013; 4(1), 1-26.
[17]   Fuller, E.N., Schettler, P.D., and Giddings, J.C. A new methode for prediction of binary gas-phase diffusion coefficients. Ind. Eng. Chem., 1966, 58(5), 18-27.
[18]   Berning, T., and Djilali, N. A 3D, Multi-Phase, Multicomponent Model of the Cathode and Anode of a PEM Fuel Cell. J. Electrochem. Soc., 2003, 150(12), A1589-A1598.
[19]   Maher A.R. Sadiq Al-Baghdadi. Novel design of a disk-shaped compacted micro-structured air-breathing PEM fuel cell. Int. Journal of Energy and Environment, 2012; 3(2), 161-180.
[20]   Maher A.R. Sadiq Al-Baghdadi. Analysis of Transport Phenomena and Electrochemical Reactions in a Micro PEM Fuel Cell. International Journal of Energy and Environment, 2014; 5(1), 1-28.